Phys. Status Solidi B **253**, No. 4, 613–622 (2016) / **DOI** 10.1002/pssb.201552496

physica status solidi b
www.pss-b.com
basic solid state physics

Atomistic modeling of interfaces in III–V semiconductor superlattices

Jürgen Maier[1] **and Hermann Detz**[*,2]

[1] Center for Micro and Nanostructures, TU Wien, Floragasse 7, 1040 Wien, Austria
[2] Austrian Academy of Sciences, Dr. Ignaz-Seipel-Platz 2, 1010 Wien, Austria

Received 31 July 2015, revised 5 January 2016, accepted 18 January 2016
Published online 15 February 2016

Keywords III–V semiconductors, atomistic modeling, interfaces, roughness, superlattices

[*] Corresponding author: e-mail hermann.detz@tuwien.ac.at, Phone: +43-1-5880136228, Fax: +43-1-5880136229

Semiconductor heterostructures are well characterized experimentally and provide a solid basis for electronic and optoelectronic devices ranging from single interface to complex superlattice structures. Yet, structural and electronic models commonly describe the material properties in a continuum approach, which neglects the crystalline structure, as well as potential local variations of the composition and resulting strain. Empirical interaction potentials provide an efficient way to model chemical bonds and therefore allow a structural description of multi-layer structures. This work provides a detailed introduction on methods to minimize the total energy of semiconductor heterostructures at an atomistic level. We present an algorithm to minimize the total energy and generate optimized interface configurations. The relaxed structures are then evaluated with respect to interfacial strain, where different strain calculation methods are evaluated and compared with experimental data.

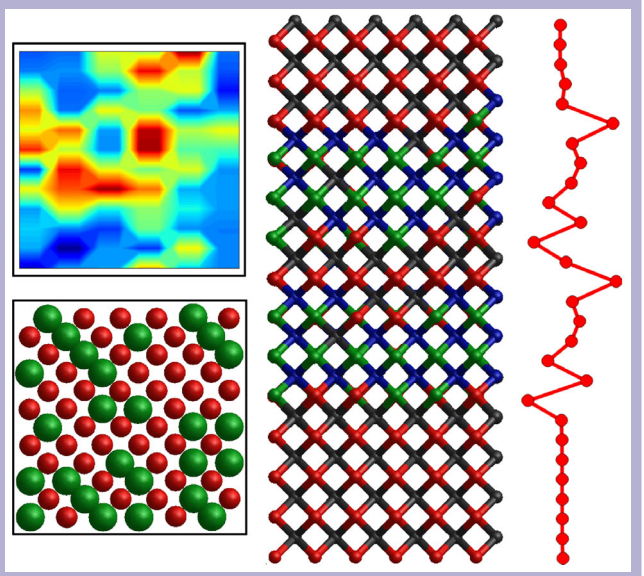

1 Introduction Semiconductor heterostructures can be considered as the foundation of many modern electronic and optoelectronic devices [1, 2]. Epitaxial growth of layer sequences or superlattices, composed of two or more materials, allows to quantum-mechanically engineer the conduction- and valence-band profile and therefore their functionality. Although not limited to, this concept has been brought to perfection in the case of III–V materials and alloys. In the simplest case, a single heterojunction can be used to form a two-dimensional electron gas, as applied in high-electron mobility transistors (HEMTs). Yet, the complexity of such structures is not limited, ranging from simple superlattices for infrared photodetectors to elaborate active region designs in the case of a quantum cascade laser (QCL) [3, 4]. All of these examples share the fact that the interface quality is one of the key issues leading to high-performance devices, as strain or roughness can significantly alter device characteristics [5, 6]. This led to detailed experimental studies on interfacial strain or roughness, particularly in InAs/GaSb and InAs/AlSb heterostructures [6–8]. Although microscopy techniques are pushed to their limits, such measurements only reveal averaged

values, but cannot completely reproduce the local atomic structure.

Despite their importance, interfaces are an often neglected point in device simulations. *Ab initio* density functional theory (DFT) methods allow an accurate description of material properties, but are not practical to simulate whole functional units for devices [9], as they are presently limited to a few thousand atoms due to the required computational effort. Therefore, the quantum mechanical behavior of device structures is commonly modeled via self-consistent Schrödinger–Poisson solvers within the envelope function approximation, where interfaces are treated to be an abrupt transition from one material to another with respect to their electronic properties like the bandgap, effective mass, etc. [10, 11]. Furthermore, the material is assumed to be a homogeneous solid. The approximation can be justified often, as even sub-monolayer thicknesses lead to an accurate description of eigenstates [12]. Yet, roughness-induced carrier scattering or alterations of the quantum-mechanical potential due to local strain are beyond the scope of such models.

Atomistic models provide the missing link to treat length scales, which are large enough to describe interface roughness, local composition variations, and related strain, while keeping the crystalline geometry of semiconductor materials. This allows detailed structural models of semiconductor heterojunctions. Chemical bonds between the individual atoms are modeled through empirical interaction potentials [13, 14], also called force fields, which allow a dramatic reduction of the computational effort, compared to DFT. Such models were successfully applied for structural simulations of Si, $Si_{1-x}Ge_x$, as well as to III–V materials and their alloys [15–17]. Recently, even the behavior of dopant atoms in III–V materials was investigated on an atomistic scale [18]. Apart from strain distributions in single quantum dots, this method was not yet applied to layered heterostructures or superlattices [19].

In this work, a novel atomistic simulation tool is presented that allows accurate modeling of multi-layer heterostructures and their interfaces. Section 2 contains a description of the basic concepts used in the simulation. Section 3 gives a detailed introduction to the algorithm used to create energetically optimized heterojunctions. Finally, Section 4 shows evaluation methods for the corresponding interface configurations with respect to their atomic structure and the introduced strain, whereat for the latter different computation methods are compared. Achieved simulation results are then compared to measurements to determine the accuracy of the presented tool.

2 Modeling method

Atomistic simulations, as summarized in Section 1, are an efficient and versatile tool to study structural properties of semiconductor materials. Empirical interaction potentials provide a level of abstraction, which allows to extend the length scales within the simulation box to several nanometers and therefore study heterostructure geometries.

This section outlines the used modeling method, starting with a description of the initial geometry of the simulation box. The following paragraphs summarize the empirical interaction potentials as well as the Metropolis Monte Carlo (MMC) solver, which are used to relax and evaluate III–V heterostructures.

2.1 Initial geometry

Simulations are carried out on a three-dimensional superlattice structure with a zincblende lattice. The modeled structures correspond to cuboids with an edge length of six unit cells for the in-plane directions. The length perpendicular to the layers depends on the amount of films and their individual thicknesses. For an overall amount of, e.g., five films, each with a thickness of two unit cells, the whole simulation box has an edge length of ten unit cells perpendicular to the layers, thus totaling to 2880 atoms. Internally, the single atoms can be uniquely determined either by their accurate position in space or by their atomic layer numbers. For a random atom A, the first one is displayed as vector $\boldsymbol{A_s} = (x, y, z)_s;\ x, y, z \in \mathbb{R}$ and the latter as vector $\boldsymbol{A_c} = (i, j, k)_c;\ i, j, k \in \mathbb{N}^0$ in $\langle 1\,0\,0 \rangle$ directions. In addition, we will use $(*, *, k)_c$ to address the kth layer in growth direction, i.e., all atoms A with $\boldsymbol{A_c} = (l, m, n)$ having $n = k$, throughout this article. Figure 1a shows the atoms of the first unity cell (top view) with their corresponding coordinates. Figure 1b depicts an interface in the initial structure; the film below the interface in growth direction is called *bottom film* and the one above *top film*, whereat the first atomic layer of the top film $(*, *, k)_c$ is additionally described by the term *interface layer*.

The in-plane lattice constant (directions [100] and [010]) of the generated superlattice structure is kept constant in all films, independent of the used material, and is determined as the relaxed lattice constant of the lowermost film (a_S), in analogy to the substrate lattice constant for pseudomorphically grown layers. The perpendicular one, i.e., in growth direction [001], however, is calculated for each film separately following term 1, where a_F represents the relaxed lattice constant and C_{11}, respectively, C_{12} the corresponding elastic constants of the III–V material used in the current film [20].

$$a_\perp = a_F + (a_F - a_S) * \frac{2\,C_{12}}{C_{11}}. \tag{1}$$

This initial adaption of the perpendicular lattice constant is not mandatory, because it would be achieved anyway during the relaxation process, however, it helps to reduce the simulation time significantly.

Generating the whole simulated structure in the beginning yields the possibility to apply periodic boundary conditions in all three dimensions. This implies that the simulated multi-layer structure is a cut-out of an infinite superlattice. This simplification, however, prevents a direct simulation of epitaxial growth, as there is no free surface, where additional atoms could be placed. The influence of anion dimer rows at a reconstructed surface under real growth conditions is therefore not considered in this simplified model [21].

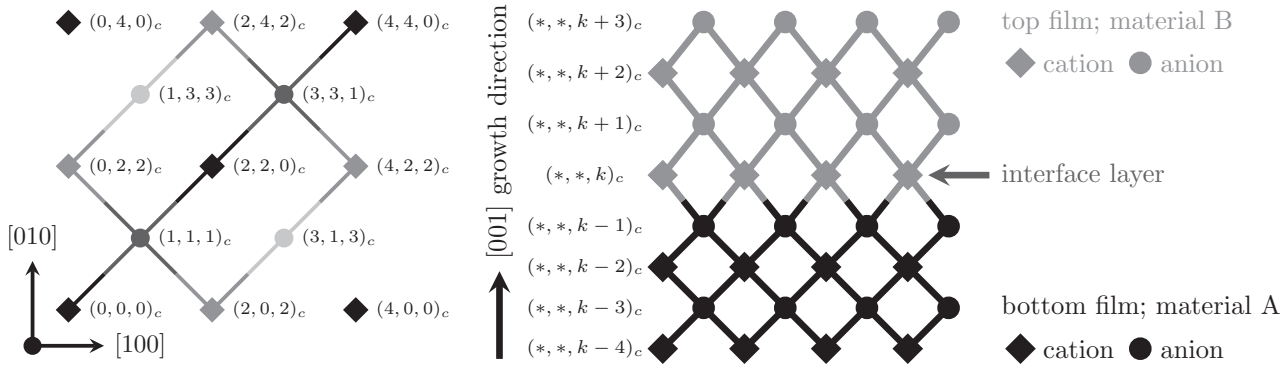

a) Atom coordinates in first unit cell b) Initial interface configuration

Figure 1 (a) Atoms of the first unit cell (top view) and their internal coordinate representation $(i, j, k)_c$ showing the atomic layer number in ⟨100⟩ directions. Diamonds represent cations and circles anions. The brighter the symbols, the higher the coordinate in [0 0 1] (growth-) direction. (b) A III–V interface in the initial structure. The film below the interface is called *bottom film*, the one above *top film*. The first layer of the latter is furthermore referenced as *interface layer*.

2.2 Empirical interaction potentials The simulations in this work are based on the empirical Tersoff potential, which was first developed for elementary semiconductors [13]. Attractive and repulsive forces are modeled with decaying exponential functions, which are fitted to reproduce the correct bond length and energy. Additional terms take all nearest neighbors and the respective bond angles into account to ensure tetrahedral bonding in a zincblende crystal lattice.

This potential was later adapted to the most common III–V materials [16, 19, 22]. [1] Although all of these parameter sets were fitted for binary compounds, the extension to ternary alloys was proven to be a good approximation with typical errors around 5% concerning hydrostatic deformations and around 10% in the case of shear stress [17].

Structural models using the Tersoff potential were also found to reproduce the experimentally observed bimodal bond length distribution random ternary alloys correctly [22, 24]. Pronounced bond deformations were found in the case of CuPt-ordered alloys, resulting in built-in strain up to −1.8% in the case of soft alloys like $GaAs_{1-x}Sb_x$.

Due to their simplicity, empirical potentials allow significantly larger simulation boxes, compared to DFT models. They are therefore ideal for structural analysis and strain evaluation in heterostructures.

2.3 Metropolis Monte Carlo (MMC) relaxation Another important part of the simulation is the relaxation of the superlattice structure where the MMC scheme is used. Trial moves are evaluated with respect to their energy gain, whereat moves reducing the total energy are always accepted. Moves increasing the energy may be accepted at a finite probability, by comparing a random number with an Arrhenius term. This method was proven to lead to reliable convergence in the case of bulk material [25, 17]. The acceptance probability can be further reduced in order to match experimental data regarding the thermal expansion coefficient [26].

To relax a structure, single atoms are displaced in a random direction by a random amount in the interval $[0, d_{max}]$. As d_{max} decreases also the energy gain achieved by a single move decreases and therefore also the convergence speed, however, the optimal energy is approached more accurately. Figure 2 shows a comparison of convergences for identical starting conditions but different values of d_{max}, whereat all data stem from single simulation runs. Averaging in the case of a constant d_{max} would not lead to a qualitative difference, yet traces with variable d_{max} can not directly be compared due to the randomness of d_{max} reduction events. Two traces in Fig. 2 were achieved with fixed values for d_{max} with a relation of 1–1000. With the higher d_{max} the energy converges faster, however, with the smaller one the results are more

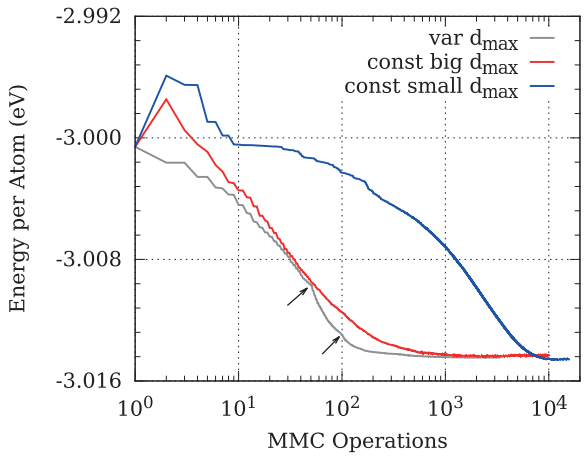

Figure 2 Convergence comparison of the relaxation algorithm twice with constant d_{max} (relation big:small 1000:1) and once with decreasing d_{max}, which approaches a suitable configuration in the shortest amount of time. The arrow in the plot indicates a reduction of d_{max} regularly followed by a steep decrease in energy. All data stem from single simulation runs with identical starting conditions.

[1] Within this work, the Tersoff parameters for Ga–As, Ga–Sb, and In–Sb bonds were taken from Ref. [23], while In–As interactions were modeled with the parameter set from Ref. [22].

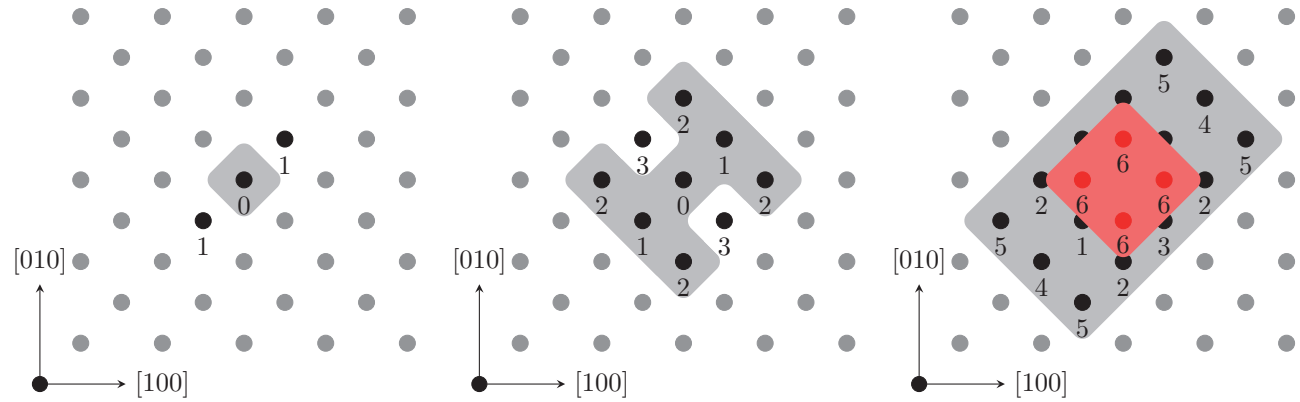

a) Randomly chosen location unsuited b) Algorithm in picking round 3 c) All considered locations

Figure 3 Site selection algorithm at different stages for layer $(*, *, k)_c$. Black dots on gray background represent already exchanged or inappropriate cations, black dots on white background cations to be checked in the current round, red ones are cations in layer $(*, *, k+2)_c$, and gray dots are cations not considered at all.

accurate. The third trace shown in the picture combines the advantages of both by steadily decreasing $d_{\max}$ during the simulation. A change of $d_{\max}$ is thereby in general followed by a steep decrease of the energy; two of these points are marked in the picture by arrows. The convergence might be improved by optimizing the points in time and the amount that $d_{\max}$ is decreased, which is, however, not within the scope of this work.

The second class of trial moves are scaling operations, which affect the simulation box partly or as a whole. These trial moves are discussed in more detail in Section 3.2.

3 Energetically optimized heterojunctions

The interfaces in the initial structure are perfectly flat, in contrast to grown samples, where always a certain roughness can be observed. To achieve realistic results, it is therefore essential to also introduce some sort of roughness in the simulation. The creation process will be described in detail in the next paragraphs. As criteria for the quality of a single configuration, the overall energy was chosen, i.e., the one with the lowest energy is determined best.

Algorithm 1: Interface Creation Procedure: Atoms are substituted, followed by local MMC relaxation. Multiple sites are evaluated with respect to the energy gain, before the optimum crystal configuration is chosen and generated.

```
foreach interface do
    foreach atom to insert do
        Site Selection;
        Substitution of Cations and Anions;
        Local Relaxation and Evaluation;
        for i = 1 to n do
            Surface Diffusion Simulation;
            Substitution of Cations and Anions;
            Local Relaxation and Evaluation;
        end
        Optimum Site Determination;
    end
    Growth-Induced Anion Tail;
end
```

3.1 Interface roughness

The interface roughness is created by changing a fixed amount of cations in the top film of an interface to ones of the bottom film; in our case an overall amount of 3/4 of a monolayer. The amount of anions is not fixed but depends on the created interface structure, as discussed in the following paragraphs. The value of 3/4 was chosen to mimic the vacancy structure of 2×4 reconstructed InAs surfaces under growth conditions and to investigate, if such features translate into characteristic roughness at superlattice interfaces [27].

In the following, the term *inserting cation* will be used for this procedure despite the fact that no new cations are introduced. Algorithm 1 gives an overview over the whole procedure; the single phases mentioned there will be described in detail in the following.

Site selection The algorithm first picks a random cation inside the interface layer $(*, *, k)_c$ and checks, if it is part of the top film. If that is the case, a valid position was found, and the algorithm proceeds to *Substitution of Cations and Anions*. Otherwise, the surrounding of that lattice site is searched for a cation belonging to the top film, which can be substituted. New positions are preferentially searched along the $\langle 1\,\bar{1}\,0 \rangle$ axis, which correspond to the fast diffusion direction on reconstructed III–V surfaces. Figure 3a–c shows the site selection procedure whereat each cation is assigned to a specific picking round, which is indicated by the numerical index. Only after all locations in round n turned out inappropriate, those in round $n+1$ are considered. If the first five rounds did not render a suitable position in layer $(*, *, k)$, the algorithm proceeds to layer $(*, *, k+2)$, where four additional

positions are available, as outlined in Fig. 3c. At the beginning of a new round the first position to check is chosen randomly, all remaining locations are cycled in clockwise direction starting from there.

Substitution of cations and anions As soon as a suitable cation in position $(i, j, k)_c$ was found, it is converted to one of the bottom film. To model group V elements rich growing atmosphere, as it is the case in III–V epitaxial growth, anions are also changed as soon as two fitting cations are in neighboring spots along the $\langle 1\,1\,0\rangle$ axis. More specifically if the cation in $(i+2, j+2, k)_c$ / $(i-2, j-2, k)_c$ is also part of the bottom film, the anion in $(i+1, j+1, k+1)_c$ / $(i-1, j-1, k+1)_c$ is changed to one of the bottom film too. If multiple cation, respectively, anion atoms are used (e.g., in ternary materials) one is chosen randomly.

Local relaxation and evaluation The space around the newly created interface roughness parts (four atomic layers in each direction) is allowed to relax using a short MMC run. In contrast to the later described relaxation of the whole structure, no scaling in growth direction is carried out here because this step would effect whole layers and not only the surrounding of the newly introduced atom.

After the energy of the interface was calculated and stored for later comparisons, the changes to the superlattice structure are undone, even for the initial placement, such that all following diffusion steps use the same starting point.

Surface diffusion simulation When an atom adsorbs at the semiconductor surface during growth, its thermal energy allows certain movement to search for the energetically best position. This is modeled by searching for further suitable cation locations across the interface. The movement direction is chosen randomly by picking one value from $\{[110], [\bar{1}\bar{1}0]\}$ and one from $\{[\bar{1}10], [1\bar{1}0]\}$.[2] When searching for the next position one of the chosen directions is picked, whereat the one from the first set is taken with a probability of 25% and the direction of the latter set with a probability of 75%. The relation of 3/1 was extracted from the aspect ratio of GaAs islands on a 2×4 reconstructed surface [28]. The next cation that is encountered along the selected direction is then checked for its suitability, i.e., if it is part of the top film and can be changed. If this is not the case, the procedure is repeated until a suitable position has been found. During this process, it is even possible for the cation to switch layers when encountering existing structures [$(*, *, k)_c \rightarrow (*, *, k+2)_c$] or leaving them [$(*, *, k)_c \rightarrow (*, *, k-2)_c$], yielding the possibility to create three-dimensional structures dynamically.

Optimum site determination After a predefined amount of different locations for a single cation has been tried, the energetically most favorable configuration is identified by comparing the calculated energy values. It is then generated again, i.e., type and position of all atoms are set as they were in that configuration, and afterward made permanent, such that all following simulation steps use this modified structure as initial condition.

Growth-induced anion tails Both epitaxial techniques, molecular beam epitaxy and metal-organic chemical vapor deposition, which are used for the fabrication of III–V semiconductor heterostructures, take place under non-equilibrium conditions. During the growth of layered heterostructures, the surface is commonly stabilized through excess group V flux. The high vapor pressure of group V species compared to group III metals, particularly when used as tetramers, limits the abruptness of interfaces and can lead to composition gradients within the following layer [29–31].

To provide a realistic description of superlattice structures, the model described here also allows decaying anion fractions, which are generated independent of the interface optimization process. In this simplified model, the first anion layers of the top film [$(*, *, k+1)_c$ and $(*, *, k+3)_c$ in Fig. 1] should contain a certain amount of anions of the bottom one. This is achieved by changing the type of a certain amount of the anions belonging to the top film. Good results have been achieved with a share of 17% in layer $(*, *, k+1)_c$ and 8% in layer $(*, *, k+3)_c$.

Algorithm 2: Structure Relaxation. The simulation box is relaxed through iterations of scaling operations and MMC-based displacements of single atoms. The maximum displacement $d_{\max}$ is refined whenever the energy gain is reduced below a certain level $f(d_{\max})$. Increasing the parameter m improves the precision and is therefore determined based on the desired accuracy of the final energy value.

```
for i = 0 to m do
    repeat
        for i = 0 to n do
            scale in growth direction;
            Metropolis Monte Carlo relaxation;
        end
    until energy gain < f(d_max);
    reduce d_max;
end
```

3.2 Relaxation To relax the modified structure, the earlier described MMC approach in combination with compression/expansion of parts of the superlattice in growth direction, as outlined in Algorithm 2, is used. The latter mechanism scales the spacing between a range of randomly chosen layers $[(*, *, a)_c$ with $a \in [k, k+m]]$ by a random amount (scale $\in [1-\epsilon, 1+\epsilon]$), as sketched in Fig. 4. The limits of the scaling operation may but do not necessarily coincide with individual films or interfaces. To perform the scaling, a unique reference atom B in layer $(*, *, k-1)_c$ with $\boldsymbol{B_s} = (u, v, w)_s$ and $\boldsymbol{B_c} = (i, j, k-1)_c$ is required. The out-

[2] This is carried out exactly once for each cation to prevent going back and forth on the same locations.

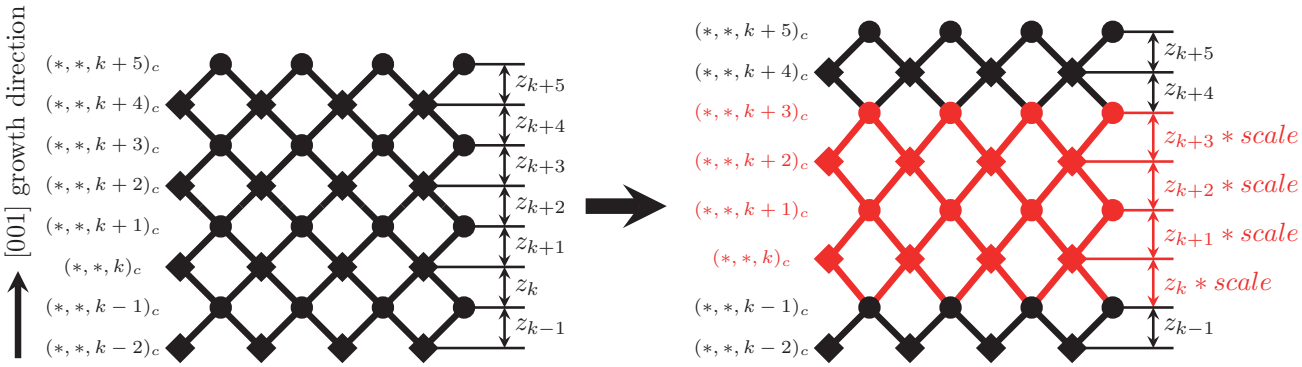

Figure 4 Scaling of layers $(*,*,a)_c$ for $a \in [k, k+3]$ with a scale value of scale = 1.2. The scaled range contains a random range of crystal planes and therefore does not necessarily correspond to the predefined superlattice films.

of-plane coordinate of this atom will be later used as reference value for the displacement computation. This approach has to be used because the scaling is executed on the already relaxed superlattice. Otherwise, the relative positioning of the single atoms between each other would be destroyed. B was defined as the atom with the smallest in-plane coordinates, i.e., the one that fulfills the conditions $i \leq f$ and $j \leq g$ for all atoms $C \in (*,*,k-1)_c$ with $\boldsymbol{C_c} = (f, g, k-1)_c$. The new position $\boldsymbol{A}_{s,\text{new}}$ for each atom $A \in (*,*,a)_c$ with $a \in [k, k+m]$ is then computed from its original position $\boldsymbol{A}_s = (x, y, z)_s$ as

$$\boldsymbol{A}_{s,\text{new}} = (x, y, w + [z - w] * \text{scale}). \tag{2}$$

The layers $(*,*,a)_c$ with $a > k+m$ also have to be shifted accordingly, to ensure that the distance between these layers and the scaled ones stay the same.

Both procedures, MMC and scaling, are carried out in alternation until the achieved energy gain over the last n iterations is below a certain value $f(d_{\max})$, in our case $d_{\max}/10$. Afterward $d_{\max}$ is reduced and the relaxation is continued, yielding very fine grained results, as already described in Section 2.3.

3.3 Interface optimization When only little energy gains are achieved by relaxation, it is tried to reorganize the interface roughness once more to find an energetically even better configuration. In detail random interface roughness cations are picked by the algorithm if they are movable. This is only the case if the surrounding cations in layer $(*,*,k+2)_c$ (depicted as red dots in Fig. 3c) where the checked cation corresponds to the atom with label 0) are not part of the bottom film. If that is the case, the cation is not part of a bigger structure and can be moved in the same fashion as described in paragraph *Surface Diffusion Simulation*. After all interfaces have been reorganized, the whole structure is again relaxed. This procedure is carried out until the energy gain achieved is below a defined limit.

4 Results This section discusses simulation results in detail and compares them to experimental data. All results depicted here were achieved by simulating a five-layer GaSb/InAs structure. The combination of InAs and GaSb was chosen as example since it is composed of two binary materials, which are almost lattice-matched but provides a finite amount of strain and allows different interface configurations. Finally, this material system has technological relevance for superlattice infrared photodetectors and can be considered a simplification of $In_xGa_{1-x}As/GaAs_{1-y}Sb_y$ heterostructures, which are, e.g., applied in QCLs [32, 5, 33].

4.1 Interfacial structure analysis The actual interface structure of the simulated superlattice is of major interest to understand roughness-induced scattering or local bandstructure variations, which were found to alter device characteristics [5, 34]. Three-dimensional topologies of the interface allow to investigate the placement and geometry of resulting roughness features. These can be divided into two major classes, as discussed in the following paragraphs.

In Fig. 5a,c an InAs on GaSb interface can be observed, which is very smooth, i.e., the roughness consists of only two monolayers (cation and anion). Naturally the single structures are heavily connected, forming a continuous pattern across the interface. Elongated voids along the $[1\,\bar{1}\,0]$ direction, which are filled with the material of the next film, appear due to the initial condition of substituting 3/4 of the cations in the interfacial plane. These structures resemble the trenches of a 2×4 reconstructed surface, although it has to be noted that they were generated solely based on total energy evaluation, whereas surface reconstructions in the case of III–V materials originate from anion dimers on the surface.

In contrast Fig. 5b,d shows a rough GaSb on InAs interface, i.e., only few and therefore higher (up to several monolayers) structures are visible. These are spread all over the interface with little to no connection in between.

4.2 Interfacial strain analysis To characterize interfaces systematically, in-plane and out-of-plane strain analyses are used. The big advantage of simulations compared to measurements on grown structures is, that a strain value for each single atom can be computed, yielding the possibility to investigate the strain even inside a single atom layer. Furthermore, the simulation renders it possible to calculate

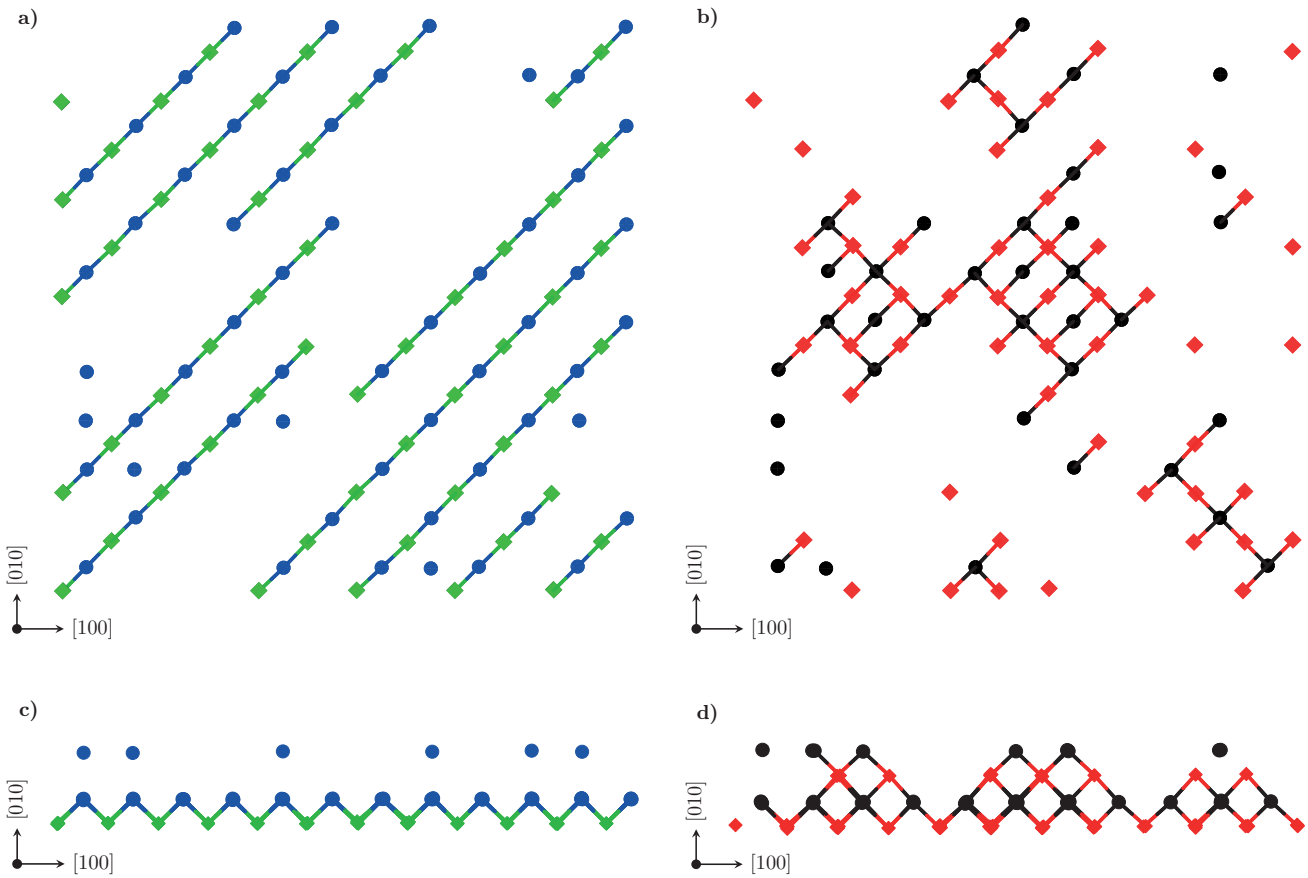

Figure 5 Smooth InAs on GaSb (a,c) and rough GaSb on InAs (b,d) interface once from top and in cross-section. Only the inserted cations/anions are shown. Floating anions without connection to other atoms have been introduced in step *Growth-Induced Anion Tail*. Green diamonds – In; blue circles – As; red diamonds – Ga; black circles – Sb.

the strain much more accurately due to the limited precision and resolution of the methods used on grown structures [6, 35, 36].

The major challenge, however, is the calculation of the strain itself, due to the fact that it is not unique. Various strain calculation methods are imaginable which will be described shortly in this subsection and afterward compared. In addition, simulation results for different structures will be presented.

4.2.1 Strain calculation To calculate a strain value for a single layer $(*, *, k)_c$, the strain of all atoms $A \in (*, *, k)_c$ is summed up and divided by the amount of atoms, i.e., the average is computed. The strain for a single atom A with $\boldsymbol{A}_c = (i, j, k)_c$ is achieved by averaging the strain values of (a subset of) its individual bonds. The strain of a single bond is finally derived by comparing a computed value (dev) to a reference one (ref) in the form

$$\text{strain} = (\text{dev} - \text{ref})/\text{ref} * 100\ [\%]. \tag{3}$$

As already mentioned, different approaches to calculate strain are available, however, all of them have this calculation method in common. They solely differ in their definition of the values dev and ref, as it will be described in the following paragraphs.

Material-dependent bond strain (MDBS) The strain achieved by this method indicates the average deformation (compression, extension) of the single bonds, whereat all four bond partners are used for the computation. The strain value for a single bond is achieved by identifying the elements of the bond atoms A and B and afterward computing the relaxed bond length for that particular material (ref). The value compared to the reference is the actual bond length which is computed as

$$\text{dev} = \|\boldsymbol{A}_s - \boldsymbol{B}_s\|, \tag{4}$$

where

$$\|(x, y, z)_s\| = \sqrt{x^2 + y^2 + z^2} \tag{5}$$

is used to display the absolute value of a vector.

Material-dependent growth strain (MDGS) This approach is very similar to MDBS, with the difference that solely the deviation in growth direction is considered. This

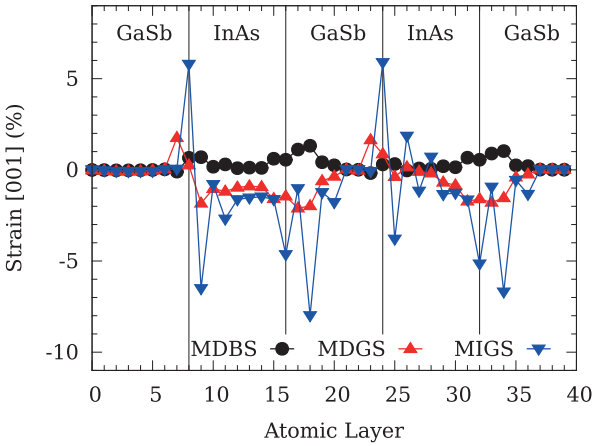

Figure 6 Strain profiles across a five-layer GaSb/InAs heterostructure computed by different strain calculation methods.

changes the calculation of dev to

$$\mathrm{dev} = \|(\boldsymbol{A}_s - \boldsymbol{B}_s) * (0, 0, 1)^T\|. \tag{6}$$

Furthermore, the reference value ref is set to one quarter of the relaxed lattice constant of the corresponding III–V material, which is equal to the share of the relaxed bond length pointing in growth direction.

Material-independent growth strain (MIGS) The final method mentioned here is often used in measurements on grown structures [35, 36] and solely uses the distance in growth direction to the bond partners in layer $(*, *, k-1)_c$, i.e. only two values are averaged to calculate the strain. The value dev is computed as shown in Eq. (6), however, ref is now material independent, i.e., constant for all appearing bonds. In zincblende lattices, as discussed in this work, it is equal to a quarter of the relaxed lattice constant of the lowermost film:

$$\mathrm{ref} = a_S/4. \tag{7}$$

4.2.2 Strain profiles across heterostructures

Results delivered by the different strain calculation methods when applied to the same structure (five-layer GaSb/InAs superlattice) are shown in Fig. 6. MDBS achieves nearly exclusively positive strain, negative one can only be observed very rarely. In the middle of a layer, i.e., away from the interface roughness, the strain value approaches 0%. This indicates that the atoms in this area are completely relaxed, meaning that the crystal structure there cannot be distinguished from one observed in a bulk material. A problem that this method shares with MDGS is, that all four bonds are considered. This circumstance makes it possible to achieve a very low absolute strain value in presence of highly strained bonds. Just consider the following example: let the strain values of the single bonds be 6.1, 2.6, −3.2, and −5.8%. By looking at these values, one can see that each single bond is significantly longer/shorter than in its relaxed configuration. By averaging these values, a final strain value of

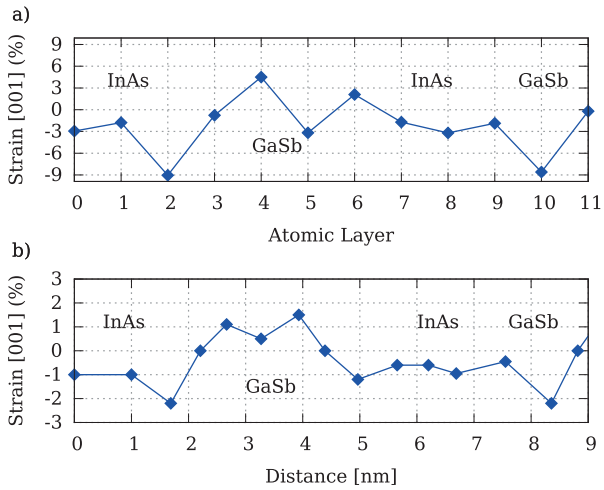

Figure 7 Comparison of (a) simulated and (b) measured (data extracted from Ref. [8]) strain profiles on a GaSb/InAs superlattice. Qualitatively, a very good matching between simulation and measurement is achieved.

$(6.1 + 2.6 - 3.2 - 5.8)/4 = -0.075\%$ is achieved, i.e., that the atom is nearly not strained at all. This shows that the MDBS method, despite yielding very valuable information about each single bond, is not very well suited for areas with huge strain variations between single bonds of an atom, as it is the case at interfaces.

Despite the fact that the calculation methods of MDBS and MDGS are quite similar, their results differ significantly. Observing the distance in growth direction only, as it is done in MDGS, makes it impossible to detect if a bond is strained or relaxed. Instead the results can only be used to determine the composition of the grown material. In detail a significant change in the out-of-plane strain can be detected between materials with differing lattice constants due to the fact that the same in-plane lattice constant is used for all films.

Finally MIGS, in the same fashion as MDGS, is only capable of detecting the layer composition but nothing about the actual strain of each single bond can be said. The main difference between these two, however, is that with MIGS solely the distance to the layer below is used and furthermore set into relation to a constant value. This leads on the one hand to a lot higher values, as shown in Fig. 6, and on the other hand to better comprehensible results. When comparing the computed strain to the results achieved by MDGS one can see, that the shapes are similar, however, the values of MIGS are far higher. One explanation is, that with MDGS all four bond partners are used for the calculation, resulting in an interference of the single strain values.

For further simulations, we chose to use MIGS as it is the method of choice when strain values for grown structures have to be determined based on TEM pictures [35, 36], making our results better comparable to measurements. Nonetheless, we think that it is not the best possible way for strain calculations because it only indicates how much the lattice constant at a given point differs from a predefined one, however, nothing can be said if a bond is actually relaxed or

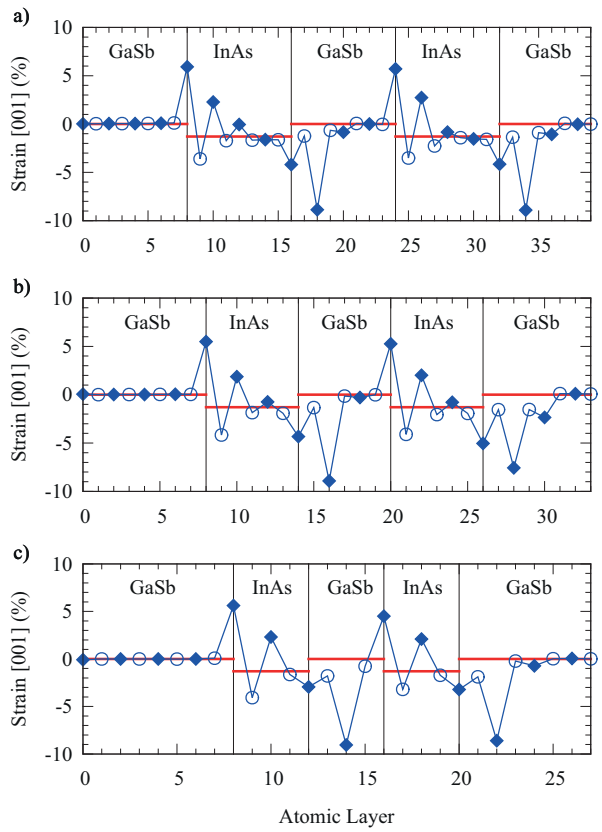

Figure 8 Strain profiles across a five-layer GaSb/InAs heterostructure. The first and last film have a constant thickness of 8 monolayers whereas the films in between are chosen with a thickness of (a) 8, (b) 6, and (c) 4 monolayers. Blue diamonds – cation layer; open circles – anion layer; red line – initial strain due to lattice constant mismatch.

strained. A comparison between simulation and measurements on grown structures is shown in Fig. 7. Qualitatively, the results fit very well, especially the strain progress at the interfaces. Slight differences may result from the fact that the simulation box is rather shallow, as compared to real structures. Another explanation could be the limited range of the used Tersoff potentials, which only take directly neighboring atoms into account.

Figure 8 shows simulation results for different film thicknesses. The top and bottom films were thereby kept at a constant thickness of 8 monolayers, whereas the ones in between were set to (a) 8, (b) 6, and (c) 4 monolayers. It can be observed that within thicker films, the nominal strain value (dashed lines), i.e., the one that is introduced at the beginning due to differing lattice constants, is successfully approached. As the film thickness decreases, the shape of the strain curves stays the same, while shifted into each other. Already with a thickness of 6 monolayers, the nominal strain is not reached any more because the strain introduced by an interface directly connects to the one introduced by the next interface.

4.2.3 Atomic layer strain map As already mentioned earlier, simulations yield the advantage that the strain

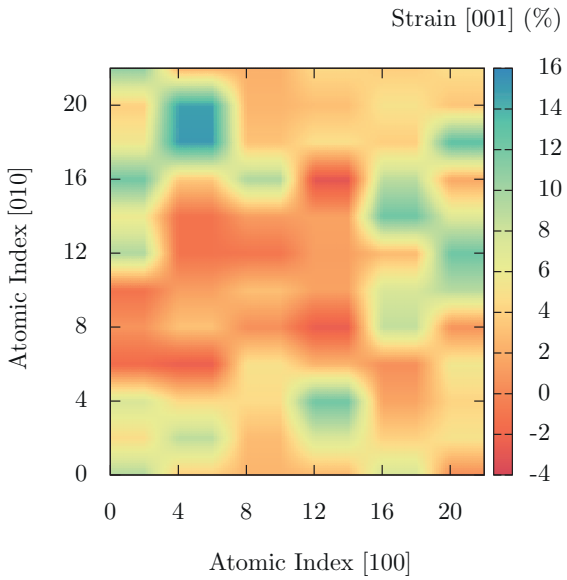

Figure 9 Strain inside a single atomic layer (interfacial layer of Fig. 5b). It can be observed that the strain is not only strongly localized but also deviates hugely across the layer.

can be computed for each single atom separately. This makes it possible to observe the strain not only per layer but also inside a single atomic layer. A lot of additional information can be achieved by this procedure compared to, for example, investigating TEM pictures of grown structures. Figure 9 shows the strain distribution inside the interfacial layer of Fig. 5b (lowermost layer). One can observe that the negatively strained areas correspond very well to regions where interface roughness is present and positively strained ones to places, where atoms of the top film are placed. This correlation allows to determine potential interface roughness solely based on a strain map.

5 Summary This work provides a detailed description of methods for atomistic modeling of semiconductor heterostructures that allow efficient construction and relaxation of multi-layer superlattice structures. The primary goal is the adequate modeling of interface roughnesses, which are locally optimized with respect to the total energy. To find the energetically best solution, several different interface configurations are tried in one run. The optimal one is later allowed to relax using a Metropolis Monte Carlo algorithm in combination with local scaling in growth direction. It turns out, that refinement steps during the relaxation improve the achieved accuracy while at the same time yielding a dramatic reduction of the required computation time.

Additionally, detailed results from InAs/GaSb heterostructures are shown, which allow insight into characteristic shapes and length scales at the different interfaces. These data can further on be used for strain analysis, where three different calculation methods are described and compared. The obtained strain distributions are found in qualitative agreement with experimental data.

Future work will be devoted on the one hand to improving the simulation tool itself, i.e., by implementing more complex mechanisms, and on the other hand to simulating more realistic structures and comparing the achieved results to measured ones.

Acknowledgements Hermann Detz is an APART Fellow of the Austrian Academy of Sciences. Furthermore, the authors gratefully acknowledge financial support by the Austrian Science Fund (FWF): P26100-N27 (H2N). The computational results presented have been achieved in part using the Vienna Scientific Cluster (VSC).

References

[1] Z. Alferov, Rev. Mod. Phys. **73**(3), 767–782 (2001).
[2] H. Kroemer, Rev. Mod. Phys. **73**(3), 783–793 (2001).
[3] C. Downs and T. E. Vandervelde, Sensors **13**, 5054 (2013).
[4] J. Faist, Quantum Cascade Lasers (Oxford University Press, Oxford, UK, 2013).
[5] C. Deutsch, H. Detz, T. Zederbauer, A. M. Andrews, P. Klang, T. Kubis, G. Klimeck, M. E. Schuster, W. Schrenk, G. Strasser, and K. Unterrainer, Opt. Express **21**(6), 7209–7215 (2013).
[6] J. Nicolai, B. Warot-Fonrose, C. Gatel, R. Teissier, A. N. Baranov, C. Magen, and A. Ponchet, J. Appl. Phys. **118**(3), 035305 (2015).
[7] J. Nicolai, C. Gatel, B. Warot-Fonrose, R. Teissier, A. N. Baranov, C. Magen, and A. Ponchet, Appl. Phys. Lett. **104**(3), 031907 (2014).
[8] K. Mahalingam, H. J. Haugan, G. J. Brown, and A. J. Aronow, Appl. Phys. Lett. **103**(21), 211605 (2013).
[9] Y.-S. Kim, M. Marsman, G. Kresse, F. Tran, and P. Blaha, Phys. Rev. B **82**(20), 205212 (2010).
[10] G. Bastard, Phys. Rev. B **24**(10), 5693–5697 (1981).
[11] I.-H. Tan, G. L. Snider, L. D. Chang, and E. L. Hu, J. Appl. Phys. **68**(8), 4071–4076 (1990).
[12] D. Chastanet, G. Lollia, A. Bousseksou, M. Bahriz, P. Laffaille, A. N. Baranov, F. Julien, R. Colombelli, and R. Teissier, Appl. Phys. Lett. **104**(2), 021106 (2014).
[13] J. Tersoff, Phys. Rev. B **38**(14), 9902–9905 (1988).
[14] M. Ichimura, Phys. Status Solidi A **153**, 431 (1996).
[15] J. Tersoff, Phys. Rev. B **39**(8), 5566–5568 (1989).
[16] D. Powell, M. A. Migliorato, and A. G. Cullis, Phys. Rev. B **75**(11), 115202 (2007).
[17] H. Detz and G. Strasser, Semicond. Sci. Technol. **28**(8), 085011 (2013).
[18] C.-W. Lee, B. Lukose, M. O. Thompson, and P. Clancy, Phys. Rev. B **91**, 094108 (2015).
[19] M. A. Migliorato, A. G. Cullis, M. Fearn, and J. H. Jefferson, Phys. Rev. B **65**(11), 115316 (2002).
[20] A. Krost, G. Bauer, and J. Woitok, High resolution X-ray diffraction, in: Optical Characterization of Epitaxial Semiconductor Layers (Springer, Berlin, Heidelberg, 1996), pp. 287–392.
[21] J. Bickel, C. Pearson, and J. M. Millunchick, Surf. Sci. **603**(1), 14–21 (2009).
[22] J. T. Titantah, D. Lamoen, M. Schowalter, and A. Rosenauer, J. Appl. Phys. **101**(12), 123508 (2007).
[23] D. Powell, Elasticity, Lattice Dynamics and Parameterisation Techniques for the Tersoff Potential Applied to Elemental and Type III–V Semiconductors, Ph.D. thesis, University of Sheffield, Sheffield, UK (2006).
[24] H. Detz and G. Strasser, J. Appl. Phys. **114**(12), 123508 (2013).
[25] C. da Silva, Comput. Phys. Commun. **153**(3), 392–396 (2003).
[26] H. Detz, Electron. Lett. **51**(18), 1455–1457 (2015).
[27] B. Z. Nosho, W. H. Weinberg, J. J. Zinck, B. V. Shanabrook, B. R. Bennett, and L. J. Whitman, J. Vac. Sci. Technol. B **16**(4), 2381 (1998).
[28] V. P. LaBella, M. R. Krause, Z. Ding, and P. M. Thibado, Surf. Sci. Rep. **60**, 1 (2005).
[29] B. Z. Nosho, B. R. Bennett, L. J. Whitman, and M. Goldenberg, J. Vac. Sci. Technol. B **19**(4), 1626 (2001).
[30] E. Luna, B. Satpati, J. B. Rodriguez, A. N. Baranov, E. Tournié, and A. Trampert, Appl. Phys. Lett. **96**(2), 021904 (2010).
[31] E. Luna, Á. Guzmán, and A. Trampert, Phys. Rev. Lett. **109**(12), 126101 (2012).
[32] H. J. Haugan, G. J. Brown, and L. Grazulis, J. Vac. Sci. Technol. B **29**(3), 03C101 (2011).
[33] Z.-B. Tian, T. Schuler-Sandy, and S. Krishna, Appl. Phys. Lett. **103**(8), 083501 (2013).
[34] C. Ndebeka-Bandou, F. Carosella, R. Ferreira, and G. Bastard, Appl. Phys. Lett. **102**(19), 191105 (2013).
[35] R. Bierwolf, M. Hohenstein, F. Phillipp, O. Brandt, G. E. Crook, and K. Ploog, Ultramicroscopy **49**(1–4), 273–285 (1993).
[36] K. Du, Y. Rau, N. Y. Jin-Phillipp, and F. Phillipp, J. Mater. Sci. Technol. **18**(02), 135 (2002).